J. Fluid Mech. (2001), *vol.* 428, *pp.* 185–212. Printed in the United Kingdom

Simulations of bypass transition

By R. G. JACOBS AND P. A. DURBIN

Mechanical Engineering Department, Stanford University, Stanford, CA 94305-3030, USA

(Received 28 September 1999 and in revised form 24 July 2000)

Bypass transition in an initially laminar boundary layer beneath free-stream turbulence is simulated numerically. New perspectives on this phenomenon are obtained from the numerical flow fields. Transition precursors consist of long backward jets contained in the fluctuating *u*-velocity field; they flow backwards relative to the local mean velocity. The jets extend into the upper portion of the boundary layer, where they interact with free-stream eddies. In some locations a free-stream perturbation to the jet shear layer develops into a patch of irregular motion – a sort of turbulent spot. The spot spreads longitudinally and laterally, and ultimately merges into the downstream turbulent boundary layer. Merging spots maintain the upstream edge of the turbulent region. The jets, themselves, are produced by low-frequency components of the free-stream turbulence that penetrate into the laminar boundary layer. Backward jets are a component of laminar region streaks.

A method to construct turbulent inflow from Orr–Sommerfeld continuous modes is described. The free-stream turbulent intensity was chosen to correspond with the experiment by Roach & Brierly (1990). Ensemble-averaged numerical data are shown to be in good agreement with laboratory measurements.

1. Introduction

Transition to turbulence by way of Tollmien–Schlichting waves is a slow process. These waves are only weakly unstable in consequence of a subtle viscous mechanism; near the upper branch they grow on the slow time scale $\delta/URe_{\delta^*}^{2/5}$ (Drazin & Reid 1995). Instability occurs at $Re_{\delta^*} \sim 500$, with transition taking place on the order of 20 times farther downstream. Any mechanism that produces growth on the inertial time scale δ/U will overwhelm the orderly process of transition via Tollmien–Schlichting waves. Under free-stream turbulence intensities of order 1% or more it is observed experimentally that transition occurs rapidly, bypassing the Tollmien–Schlichting route. Inertial-time-scale processes apparently come into play, but their origin and nature are not at present known.

Bypass transition falls somewhere between turbulence and transition. It is stochastic by nature, and so lies within the province of statistical fluid dynamics. It entails rapid amplification of boundary layer perturbations, and so lies within the arena of hydrodynamic instability. It is provoked by external perturbations, and so is an instance of boundary layer receptivity. These various perspectives have led to attempts on the problem via linear stability theory (Reshotko 1976), nonlinear stability analysis (Li *et al.* 1998), turbulence modelling (Saville 1996), non-homogeneous rapid distortion theory (Hunt & Carruthers 1990; Leib, Wundrow & Goldstein 1999), and the like.

Progress in this field has been hampered by a lack of detailed data and phenomenological information. The intent of the present paper is to contribute to the available

data on bypass transition and to provide depictions of the eddies and interactions that occur during the process of bypass transition. The particular case under study here is transition induced by free-stream grid turbulence. Experiments were performed on a parallel computing platform by direct numerical simulation (DNS) using the incompressible Navier–Stokes equations. The qualitative and quantitative data to be presented provide views of the process of coupling between free-stream turbulence and boundary layer eddies. These computer studies complement laboratory experiments, both in their degree of resolution and in their comprehensiveness.

1.1. *Bypass mechanisms*

There are three regions of concern to studies of bypass transition: the buffeted laminar boundary layer; the region of intermittent turbulent spot formation; and the fully turbulent boundary layer. In the buffeted laminar layer the skin friction is only slightly elevated by the free-stream turbulence, and the boundary layer remains stable to perturbations. In this region, shear filtering and non-modal, shear amplification lead to elongated streaks in the u-component of velocity fluctuations.

In the intermittent region, localized perturbations trigger instabilities that ultimately evolve into patches of irregular motion. Patches of irregular motion in the laminar region will be termed turbulent spots. However, their character differs from the classic Emmons spots (Van Dyke 1982); they are not downstream-pointing arrowheads. They originate near the top of the boundary layer, being generated by free-stream eddies; Emmons spots are usually stimulated by forcing at the wall. These distinctions have led to the terminology 'top-down' and 'bottom-up' spots. Bypass transition occurs via top-down spots. Once fully formed, these spots spread laterally and grow longitudinally. They overtake the main turbulent region and thereby maintain its upstream edge. That edge is irregular, consisting of juxtaposed zones of laminar motion, in which laminar streaks are usually visible, and zones of fully turbulent motion.

In the last region of concern to bypass transition, the boundary layer is turbulent across its entire span. The present numerical flow fields permit an examination of low-intensity precursors to the appearance of turbulent spots; they enable the spatial and temporal evolution of streaks in the laminar boundary layer to be visualized; and they allow spots in the transitional boundary layer to be followed from inception to absorption into the fully turbulent zone.

One of many outstanding issues in bypass transition is the receptivity process (Reshotko 1976). Linear, high-Reynolds-number theory for quasi-parallel shear flow shows that free-stream vortical perturbations do not couple to boundary layer modes (Kerschen 1991). At finite Reynolds number, low-frequency modes can penetrate the boundary layer, but they are generated by viscously decaying free-stream motions and cannot lead directly to instability (Jacobs & Durbin 1998). The present simulations show that once they enter the boundary layer, these low-frequency perturbations produce even lower frequency boundary layer modes. These very low-frequency perturbations are then amplified and elongated in the streamwise direction by the shear. They develop into streaks in the streamwise velocity contours. The streaks grow in strength through the rapid-distortion mechanism of shear amplification (Phillips 1969). Essentially, streamwise elongated perturbations, having small streamwise pressure gradients, grow by vertical displacement of mean momentum. The magnitude of the velocity perturbations seen in the present study sometimes reaches 25% of the free-stream velocity, similar to levels seen in experiments of Alfredsson & Matsubara (1996).

Whether or not they play a role in bypass transition, the streaks in the laminar boundary layer are an intriguing phenomenon. The formation of elongated contours

of u-component velocity seems to be a ubiquitous feature of strongly sheared disturbances (Lee, Kim & Moin 1990). Rapid-distortion theory shows how streamwise elongated disturbances ($k_1 \to 0$) are subjected to prolonged growth of the streamwise velocity perturbation (u'). But this theory does not select a spanwise wavelength; hence, it does not predict boundary layer streaks *per se*.

A linear theory of streaks in laminar flow has been developed by Butler & Farrell (1992), Andersson, Berggren & Henningson (1999), Luchini (2000) and others. These authors show that in a stable, viscous boundary layer disturbances ultimately decay, even though they can experience substantial shear amplification. At any given location certain disturbances have sustained the maximum net growth. These fall in a narrow range of spanwise wavenumbers. Again, the disturbances are dominated by the streamwise velocity component and are elongated in the streamwise direction by the rapid distortion mechanism. However, now spanwise streaky structure is predicted because the largest perturbations are supposed to lie in the band of spanwise wavenumbers that shows maximum amplification. The dominant wavelength of linear theory can be considered an estimate of the average spacing between the streaks observed in the DNS: this estimate is consistent with the present results. However, the DNS streaks are far from periodic or sinusoidal.

Streaks are almost certainly identical to so-called 'Klebanoff modes'. The statistical properties of the laminar region streaks in the present numerical simulation are in good accord with experimental measurements of Klebanoff modes. But they are not modes, in the sense of being eigenfunctions; they are disturbances forced by free-stream turbulence and magnified by the boundary layer shear. Klebanoff modes are an ensemble-averaged view of the instantaneous streaks.

What the connection of u-component streaks in the laminar layer to transition is, has to date been, uncertain. It was recently proposed that spanwise periodic streaks might undergo a secondary, sinuous instability, which subsequently would develop into turbulent spots through a tertiary instability (Alfredsson & Matsubara 1996; Elofsson, Kawakami & Alfredsson 1999). Our simulations showed no evidence of sinuous, or other prefatory streak instability; the streaks usually persist right up to the edge of the turbulent region. It is more likely that certain features of individual streaks make the boundary layer receptive to perturbation by free-stream eddies. Reddy *et al.* (1998) proposed that spanwise inflectional profiles are the origin of breakdown. This mechanism was explored, but we found no evidence of it under the conditions of the present simulations.

It appears that perturbations first enter the boundary layer in a region where a streak takes the form of a long, intense 'backward jet' (Wu *et al.* 1999). The term backward jet refers to the velocity relative to the mean local mean, $U(x, y, z, t) - \bar{U}(x, y) < 0$; the total velocity $U(x, y, z, t)$ is not reversed in these structures. These jets exist throughout the boundary layer, but they only couple to small-scale free-stream turbulence when they are in its upper portion. In this role, streaks overcome the sheltering effect of the mean shear by introducing three-dimensional, low-frequency, unstable flow near the top of the boundary layer. This is acted on by free-stream eddies.

Spot precursors are localized instabilities of a single one of these jets. The jets are continually being perturbed, but instability occurs seldomly. Few localized disturbances are such that they grow rapidly into small-scale irregularities. When it occurs, this irregular motion is first observed at fine resolution. It develops in strength and eventually emerges on a coarser resolution as a 'turbulent spot'. A similar phenomenon was observed by Wu *et al.* (1999) in transition beneath periodic passing wakes. In

that case elongated streaks were precluded by the finite wake width; instead, shorter 'puffs' were observed. Breakdown was associated with backward jets, seen high in the boundary layer. Backward jets seem generally to be a link between free-stream eddies and the boundary layer – at least with zero mean pressure gradient. The breakdown is on isolated jets; streak spacing, *per se*, is irrelevant to transition.

The actual development of turbulence proceeds through the appearance of localized regions of turbulence, or turbulent spots. These form when the irregular motion triggered at the free-stream edge of the boundary layer cascades toward the wall. Once formed, spots spread laterally and intensify as they propagate downstream. Eventually they join onto a main turbulent region, thereby maintaining its upstream edge. As the spots join the main region, they form juxtaposed zones of turbulent and laminar flow, just upstream of a fully turbulent region. It appears that the growth and merging are crucial features of the bypass mechanism proper. But the spots are already developed regions of turbulence: by the stage at which the patch of irregular motion can be called a turbulent spot, the transition mechanism is already well underway. To understand the bypass route one must examine earlier stages, tracing them back to the initial coupling between free-stream turbulence and the boundary layer. Presumably that is where the crucial three-dimensional receptivity path occurs. Here and in Wu *et al.* (1999) backtracking is facilitated by numerical simulation. When a spot is observed, the simulation can be restarted at an earlier time and intermediate solution fields saved.

The observations cited in the present paper bear subjective resemblance to results of recent mathematical research by F. T. Smith and collaborators (Li *et al.* 1998, and references therein). The fact that spot precursors originate in the outer boundary layer is reminiscent of concepts of nonlinear critical layer modes. The rapid breakdown of isolated jets is suggestive of explosive growth associated with inflectional profiles, seen in nonlinear amplitude equations. Bowles & Smith (1995) consider a model of boundary layer spots in which the mean profile is represented by a linear shear joined to a constant free-stream velocity. Perturbations then consist of vorticity waves propagating on the vorticity discontinuity at the top of the boundary layer. The front of the spot is then composed of short waves, while the rear contains long, slower waves. This seems to provide a simple model for the top-down spots seen in our simulations.

The localized receptivity mechanism of Tam (1978) is very likely to be relevant to the initial coupling to free-stream disturbances. It has not escaped our attention that various stages of the transition mechanism observed in the present simulations can be connected to a wide range of analyses. In most cases the connections are subjective.

1.2. *Bypass transition simulation*

The present simulations of bypass transition provoked by free-stream turbulence use the methodology proposed by Grosch & Salwen (1978) and by Jacobs & Durbin (1998) to synthesize free-stream turbulence. The free-stream turbulence is expanded as a sum of spanwise and temporal Fourier modes, times vertical Orr–Sommerfeld modes. The Orr–Sommerfeld modes consist only of the continuous spectrum. It was first proposed by Grosch & Salwen that the continuous spectrum provides a natural basis for free-stream turbulence. Indeed, far above the boundary layer the continuous spectrum becomes a Fourier spectrum. Hence, kinematic synthesis of inflow turbulence proceeds in the same manner as is used to initiate grid turbulence simulations (Rogallo 1981). The present effort is the first to use the Orr–Sommerfeld continuous spectrum to create synthetic free-stream turbulence.

This method of inflow synthesis avoids the need to compute the evolution of grid turbulence upstream of the leading edge of the flat plate, or indeed, to compute the flow round a sharp leading edge, as was done by Rai & Moin (1993). The expansion in Orr–Sommerfeld modes enables the computation to be done in a rectangular region, with a lower no-slip wall and with a Blasius boundary layer introduced at the inlet. The advantages are that the computational domain is shortened, by avoiding the leading edge and starting with a finite thickness boundary layer, and that a more efficient computational algorithm can be used because the lower wall extends over the whole streamwise domain.

In the opening paragraph of their review on direct simulations of the Tollmien–Schlichting route to transition, Kleiser & Zang (1991) allude to "transition induced by mysterious 'bypass mechanisms'". Despite theoretical speculations cited above, bypass mechanisms have remained somewhat mysterious. The potential of direct simulation to shed light on the subject has remained largely untapped. Simulations of wake-induced transition by our group (Wu *et al.* 1999) provide intriguing views of the process.

Low-resolution simulations of transition under free-stream turbulence were performed by Yang & Voke (1995). Their grids were far too coarse to explore bypass mechanisms. A subgrid model was used in some of their computations; others were run with no model. In either case the large subgrid dissipation would prevent proper resolution of streaks, spots and their precursors. The primary conclusion of Yang & Voke (1995) was that the normal component of free-stream intensity dominates the interaction with the boundary layer. This was surmised from a thought experiment, in which the inlet turbulence was either given only a u-component or only a v-component. The former did not provoke transition, the latter did. The dominance of the v-component is a significant insight.

A proper DNS of transition under free-stream turbulence was performed by Rai & Moin (1993). Their simulation started upstream of the leading edge of a flat plate. The long computational domain imposed excessive grid requirements. This was addressed by using a three-zone grid. A coarse grid was used in the upstream and exit zones. The coarse exit-zone grid was intended to suppress turbulence fluctuations prior to imposing the outflow boundary condition. In preliminary tests, we found no need for such a sponge region with the present numerics – perhaps this is because our simulations are incompressible while Rai & Moin (1993) used a compressible code. In their main zone, Rai & Moin (1993) observed turbulence-induced transition. They found that the x-dependence of C_f was quite sensitive to grid resolution. In their most resolved computation it rose too abruptly, to a level well above the turbulent correlation. They estimated that a grid spacing of $\Delta x^+ \simeq 12$ and $\Delta z^+ \simeq 6$ was required; due to computational expense their finest resolution was $\Delta x^+ \simeq 28$ and $\Delta z^+ \simeq 10$. Based on the present simulations, the erroneous $C_f(x)$ curve computed by Rai & Moin (1993) was probably a consequence of inadequate streamwise resolution. Fields of instantaneous vorticity were discussed in terms of orderly transition mechanisms: detached shear layers, one and two-spike stages and the like. No evidence of the bypass mechanisms discussed herein was seen in their visualizations.

2. Numerical method

The incompressible Navier–Stokes equations were solved by the fractional step algorithm described in Akselvoll & Moin (1996). This is a central difference, pressure correction method, solved on a staggered grid. Convection and diffusion in the

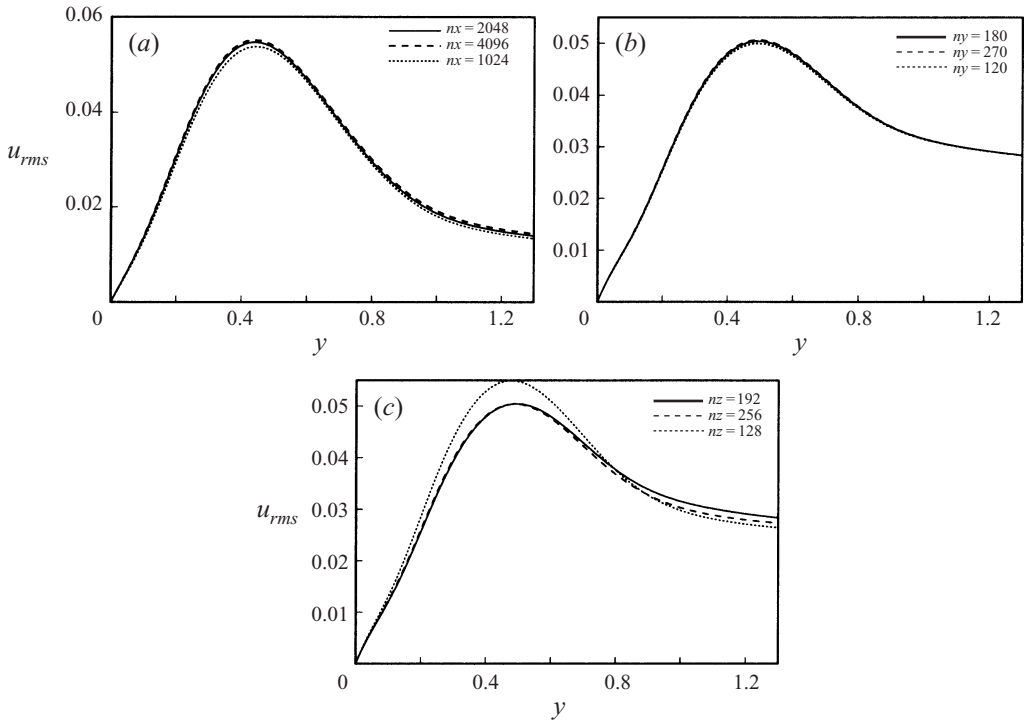

FIGURE 1. Grid resolution on 1/32 of streamwise domain. (*a*, *b*, *c*) Refinement in x, y and z, respectively.

horizontal plane are treated explicitly and solved by third-order Runge–Kutta time stepping. Diffusion is implicit in the vertical direction and convection is linearized to make it partially implicit. The implicit terms follow the Crank–Nicholson time-stepping scheme. The computer code is a parallel implementation of this algorithm by Pierce & Moin (1998). Computations were done on 128 processors of an SGI Origin 2000. A full simulation required on the order of 500 hours of CPU time per processor.

The flow domain was a rectangular box of relative dimensions $15.5 \times 1 \times 0.75$; or, in units of the inlet 99% boundary layer thickness, δ_0, it is $620 \times 40 \times 30$. The grid was uniformly spaced in the x- and z-directions and clustered near the wall in the y-direction. The uniform grid spacing in the horizontal plane enabled the Poisson equation for the pressure to be solved directly by fast Fourier transforms in x and z, and tridiagonal matrix inversion in y.

The top boundary condition was $U = 1$, $W = 0$ and $V = \mathrm{d}\delta^*_{Blasius}/\mathrm{d}x$; the laminar Blasius boundary condition on V was used throughout the domain. Capital letters here denote the total velocity. The Blasius condition was used to obtain very accurate growth rates of Tollmien–Schlichting waves in the laminar region. It was found that setting $V = 0$ or $\partial_y V = 0$ produced almost identical mean velocity and skin friction to those obtained with the Blasius boundary condition.

Spanwise periodicity was imposed. Studies conducted throughout the course of this work verified that the width of the domain was great enough to avoid spurious correlations. It especially was verified that the average streak spacing in the laminar region was uninfluenced by the lateral domain size.

The primary solutions presented herein were on a $2048 \times 180 \times 192$ grid in x, y and z. This grid gives Δx_+ of 11.7 and Δz_+ of 6.0 at the skin friction maximum; in other words, this is the coarsest resolution in + units. It was found that coarser streamwise resolution caused the skin friction to slightly overshoot the turbulent level after transition. Streamwise velocity fluctuation was the most sensitive indicator of under-resolution. Grid refinement studies were done on coarser grids to ascertain that the final grid provides satisfactory numerical accuracy. Figure 1 compares u' on the final grid to a finer and to a coarser grid. This figure shows the approach to grid independence. In order to study the effect of grid resolution these computations were on 1/32 of the streamwise domain: for instance the '4096' point computation actually used 128 points so that the Δx corresponded to 4096 points on the full domain. Each portion of figure 1 contains three curves: the solid lines are the final grid; the dashed line is finer; and the dotted line is coarser. The greatest sensitivity is to the spanwise resolution. The simulation grid appears to be satisfactory in all directions. Further verification of numerical accuracy can be found in Jacobs (1999).

2.1. *Inflow generation*

In the free stream the turbulence is isotropic. Apart from its interaction with the boundary layer, it simply decays with downstream distance. Isotropic grid turbulence can be simulated by a sum of Fourier modes with random amplitudes:

$$\boldsymbol{u}(\boldsymbol{x}) = \sum_{\boldsymbol{k}} \hat{\boldsymbol{u}}(\boldsymbol{k})\, \mathrm{e}^{\mathrm{i}\boldsymbol{k}\cdot x}. \tag{2.1}$$

As an inlet condition, $k_1 x_1$ is replaced by $-\omega t$, invoking Taylor's hypothesis and ignoring streamwise decay. With this replacement

$$\boldsymbol{u}(x=0,y,z,t) = \sum_{k_y,k_z,\omega} \hat{\boldsymbol{u}}(k_y,k_z,\omega)\, \mathrm{e}^{\mathrm{i}(k_y y + k_z z - \omega t)}. \tag{2.2}$$

For the boundary layer simulation this has to be modified to accommodate the wall. To this end, the y-direction Fourier modes are replaced by an alternative, complete basis $\phi_{k_y}(y)$:

$$\boldsymbol{u}(x=0,y,z,t) = \sum_{k_y,k_z,\omega} \hat{\boldsymbol{u}}(k_y,k_z,\omega)\boldsymbol{\phi}_{k_y}(y)\, \mathrm{e}^{\mathrm{i}k_z z}\, \mathrm{e}^{-\mathrm{i}\omega t}. \tag{2.3}$$

An appropriate basis for the wall-normal component of velocity is the Orr–Sommerfeld modes.

The general solution to the Orr–Sommerfeld equation in an unbounded flow can be decomposed into a sum of a finite number of discrete modes plus a continuum of modes. The discrete modes decrease exponentially with y in the free stream. They are not generated by free-stream turbulence. These components are not included in the inflow representation because the interest here is in bypass transition caused by external, vortical disturbances.

The continuum eigenfunctions solve

$$(\alpha U - \omega)(\phi'' - \alpha^2\phi) - \alpha U''\phi = \frac{-\mathrm{i}}{R}(\phi^{\mathrm{iv}} - 2\alpha^2\phi'' + \alpha^4\phi) \tag{2.4}$$

for an $\mathrm{e}^{\mathrm{i}\alpha x}$-dependent eigenfunction. R is the Reynolds number. Equation (2.4) is subject to the asymptotic condition that ϕ is bounded, but not zero, at infinity. At the wall, $y = 0$, $\phi = \phi' = 0$. These boundary conditions define an eigenvalue problem for the complex function ϕ and the complex eigenvalue α. An algorithm to solve

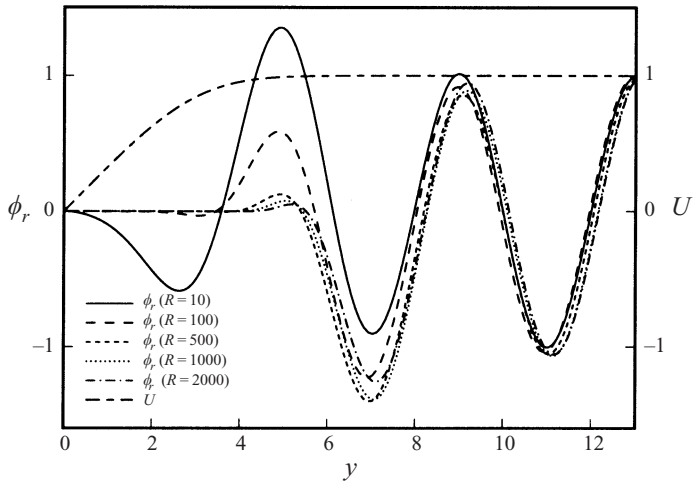

FIGURE 2. Some continuous modes of the Orr–Sommerfeld equation.

(2.4) subject to boundedness is described in Jacobs & Durbin (1998). As $y \to \infty$, the bounded solution behaves as $\phi \propto A\,\mathrm{e}^{\mathrm{i}k_y y} + B\,\mathrm{e}^{-\mathrm{i}k_y y}$ and the eigenvalue is found explicitly to be

$$\alpha = \frac{\mathrm{i}}{2}\left[\sqrt{R^2 + 4(k_y^2 - \mathrm{i}R\omega)} - R\right]. \tag{2.5}$$

The non-dimensionalization is to $U_\infty = 1$. As $\omega/R \to 0$, $\alpha \to \omega$. Typical continuum modes are plotted in figure 2. This figure shows how the modes are sinusoidal in the free stream, but are damped rapidly inside the boundary layer. This damping is caused by the mean shear flow (Hunt & Durbin 1999). Low-Reynolds-number or low-frequency modes are able to enter the sheared region; Jacobs & Durbin (1998) suggest that the penetration depth varies as approximately $(\omega R)^{-0.13}$. The small mode amplitude inside the boundary layer embodies the concept of shear sheltering.

The v-component of inlet free-stream turbulence was created by summing Orr–Sommerfeld modes:

$$v|_{x=0}(y,z,t) = -\sum_{\omega}\sum_{k_y}\sum_{k_z} A(\omega,k_y,k_z)\,\mathrm{i}\sqrt{\omega^2+k_z^2}\,\phi(\omega,k_y,R;y)\,\mathrm{e}^{\mathrm{i}k_z z}\,\mathrm{e}^{-\mathrm{i}\omega t}. \tag{2.6}$$

If the inlet disturbance were a sum of oblique Orr–Sommerfeld modes then u and w would be analogous to the above, with $\mathrm{i}\sqrt{\omega^2+k_z^2}\,\phi$ replaced by $-\phi'\cos\gamma$ and $-\phi'\sin\gamma$. The wave obliqueness suited to the present usage is

$$\tan\gamma = \frac{k_z}{\omega}$$

in which ω/U_∞ plays the role of a streamwise wavenumber and U_∞ is normalized to unity. However, oblique Orr–Sommerfeld waves contain only horizontal vorticity. In order to represent isotropic free-stream turbulence it is necessary to add vertical vorticity. In a linear analysis inside the flow domain, the vertical vorticity would be obtained by solving Squires' equation. For only representing the inlet disturbance, the vertical vorticity can be specified more simply by adding another term proportional

to ϕ' to the horizontal velocities. The forms

$$\left.\begin{aligned} u(y,z,t) &= \sum_{\omega}\sum_{k_y}\sum_{k_z} \phi'(\omega,k_z,R;y)\left[A(\omega,k_y,k_z)\cos\gamma + B(\omega,k_y,k_z)k_z\right] \mathrm{e}^{\mathrm{i}k_z z}\,\mathrm{e}^{-\mathrm{i}\omega t} \\ w(y,z,t) &= \sum_{\omega}\sum_{k_y}\sum_{k_z} \phi'(\omega,k_z,R;y)\left[A(\omega,k_y,k_z)\sin\gamma - B(\omega,k_y,k_z)\omega\right] \mathrm{e}^{\mathrm{i}k_z z}\,\mathrm{e}^{-\mathrm{i}\omega t} \end{aligned}\right\} \tag{2.7}$$

were used. The effective Reynolds number and true Reynolds number are related by $R = Re\cos\gamma$ due to the wave obliqueness to the mean flow. In the main simulation described herein, the inlet Blasius layer had $R_\theta = 106$; correspondingly $R_x = 2.55\times10^4$. The Orr–Sommerfeld modes were computed for this profile.

The construction (2.7) would satisfy incompressibility if the x-dependence were $\mathrm{e}^{\mathrm{i}\omega x}$. Continuous modes inside the flow domain behave as $\mathrm{e}^{\mathrm{i}\alpha x}$ with α given by (2.5), but $\alpha \approx \omega$ to a high degree for the modes of present interest. The objective of this inflow construction is to introduce disturbances smoothly into the flow, in order to minimize the distance over which they adjust to a sensible representation of grid turbulence. The present technique was found to be very effective. Of course incompressibility is satisfied exactly inside the flow domain; (2.7) and (2.6) serve only to produce an inlet perturbation. Computations of individual modes were in excellent agreement with (2.5) (Jacobs 1999).

In the free stream $\phi \sim \mathrm{e}^{\mathrm{i}k_y y}$ and the inflow representation can be expressed as three-dimensional Fourier amplitudes

$$\hat{u} = \frac{\mathrm{i}k_y\omega A}{\sqrt{\omega^2+k_z^2}} + Bk_z, \quad \hat{v} = -\mathrm{i}\sqrt{\omega^2+k_z^2}A, \quad \hat{w} = \frac{\mathrm{i}k_y k_z A}{\sqrt{\omega^2+k_z^2}} - B\omega. \tag{2.8}$$

The terms containing A can be thought of as the Orr–Sommerfeld modes and those containing B as Squire modes.

An isotropic spectrum was generated by letting (Rogallo 1981)

$$\left.\begin{aligned} A &= F\mathrm{e}^{\mathrm{i}\theta_1}\cos\delta, \\ B &= F\sqrt{\frac{\omega^2+k_z^2+k_y^2}{\omega^2+k_z^2}}\,\mathrm{e}^{\mathrm{i}\theta_2}\sin\delta, \end{aligned}\right\} \tag{2.9}$$

where θ_1, θ_2 and δ are uniformly distributed random angles. The functional form of F defines the energy spectrum through

$$F = \sqrt{\frac{E(\omega^2+k_z^2+k_y^2)}{4\pi[\omega^2+k_z^2+k_y^2]^2}}. \tag{2.10}$$

If ω is synonymous with k_x then multiplying (2.8) by its complex conjugate, averaging and using (2.9) gives the isotropic energy spectrum tensor

$$\overline{\hat{u}_i\hat{u}_j} = \frac{E(|k|)}{4\pi|k|^4}(|k|^2\delta_{ij} - k_i k_j). \tag{2.11}$$

The turbulent intensity, Tu, is given by

$$Tu^2 = \overline{u_0^2} = \frac{2}{3}\int_0^\infty E(k)\,\mathrm{d}k. \tag{2.12}$$

The simulations in this paper are for inlet $Tu = 0.035$ and, in §4, for $Tu = 0.07$. The

spectral shape

$$E(k) = \overline{u_0^2} \frac{L^5 k^4}{C[1 + (kL)^2]^{17/6}} \tag{2.13}$$

was used, where L is a turbulence length scale. The normalization constant is

$$C = \frac{2}{3} \int_0^\infty \frac{x^4}{[1 + x^2]^{17/6}} \, \mathrm{d}x = \frac{\sqrt{\pi}\, \Gamma(1/3)}{4\Gamma(17/6)}$$

and L is related to the integral scale $L_{11} \equiv \int_0^\infty \overline{u(x)u(x+r)}/\overline{u_0^2} \, \mathrm{d}r$ by

$$L = \frac{55C}{9\pi} L_{11}.$$

3. Results

The goal of these numerical simulations is to gain insight into the bypass transition process, not necessarily to match previous experiments. As fully resolved numerical solutions to the Navier–Stokes equations, direct numerical simulations are verified by grid refinement tests. However, comparisons to experimental data can bolster confidence in the computations. For this reason the inlet turbulent intensity was chosen in correspondence to case T3a of Roach & Brierly (1990). It would be virtually impossible to reproduce the details of the laboratory experiment, but a reasonable approximation was obtained. The inlet turbulence intensity of the simulation was 3.5%; it decayed to 0.6% by the exit. A second simulation with 7% inlet turbulence was also performed; a few results from this second case will be presented in § 4 and compared to case T3b of Roach & Brierly (1990).

An objective of the method of inflow simulation was to produce nearly isotropic grid turbulence far above the boundary layer. The isotropic relation $u' = v' = w'$ was met to within 10% inside the flow domain. The free-stream turbulence intensity follows the decay law $Tu \propto (x + x_0)^{-n}$ with $n \approx 0.71$. The integral length scale

$$L_k = -\frac{k^{3/2}}{d_x k} \tag{3.1}$$

normalized by local boundary layer (99%) thickness versus Re_x is shown in figure 3, along with Tu/Tu_{in}. The integral scale grows as $x^{0.29}$. The boundary layer thickness grows more rapidly, so the ratio plotted in figure 3 decreases with x. Transition to turbulence begins at $Re_x \approx 1.5 \times 10^5$. At that point the turbulence integral scale is about one half of the 99% boundary layer thickness. While these properties are not identical to the T3a experiment, they are sufficiently close that a fair comparison can be made.

The main simulations will be presented in three subsections: the first addresses single-point, Reynolds-averaged data; the second is on instantaneous fields; and the third presents space–time spectra. The first section is primarily a comparison to experiment. The second and third contain new results on the mechanics of bypass transition.

3.1. *Reynolds-averaged fields*

A plot of skin friction coefficient versus distance or Reynolds number provides a good overview of the onset and length of transition. The development of the skin friction, momentum thickness and shape factor are presented in figure 4. Data of Roach &

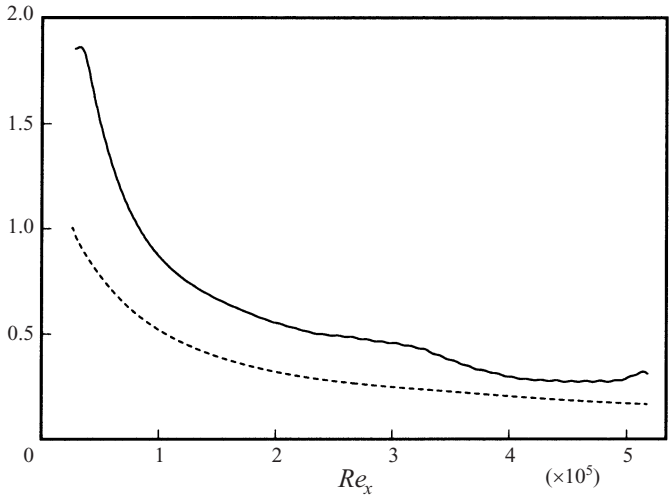

FIGURE 3. Free-stream decay. ····, Tu/Tu_{in}; ——, L/δ.

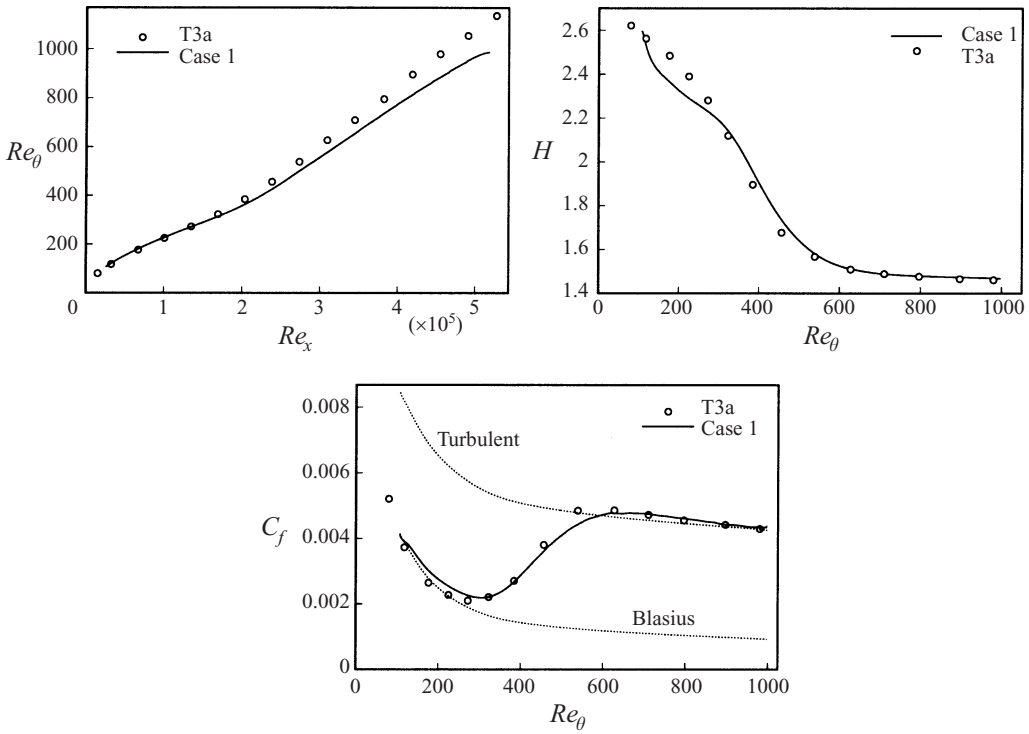

FIGURE 4. Momentum thickness, form factor and skin friction compared to data from Roach & Brierly (1990).

Brierly (1990) are included in the figure. It can be seen that the DNS and experiment develop similarly. If the onset of transition is defined as the point where C_f reaches its minimum and the completion of transition is where C_f attains its maximum, then both DNS and experiment show the onset to occur at $Re_\theta \approx 300$ and transition to be complete at $Re_\theta \approx 600$. The DNS is slightly later than the experiment in both

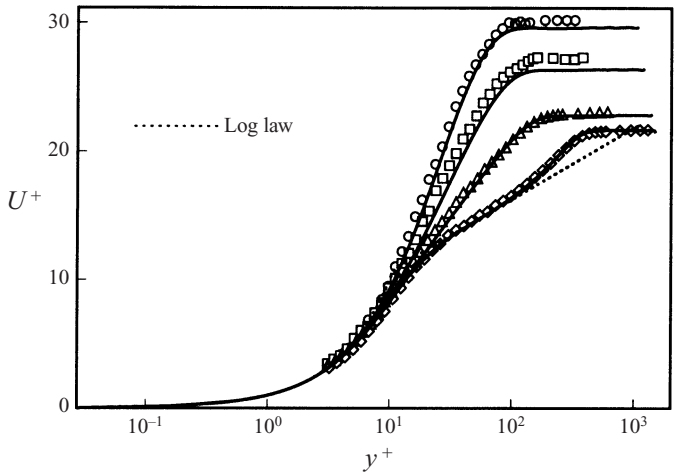

FIGURE 5. The evolution of mean velocity profiles through the laminar to turbulent transition. Data of Roach & Brierly (1990). ○, $R_\theta = 323$; □, $R_\theta = 385$; △, $R_\theta = 456$; ▽, $R_\theta = 539$; ◇, $R_\theta = 980$.

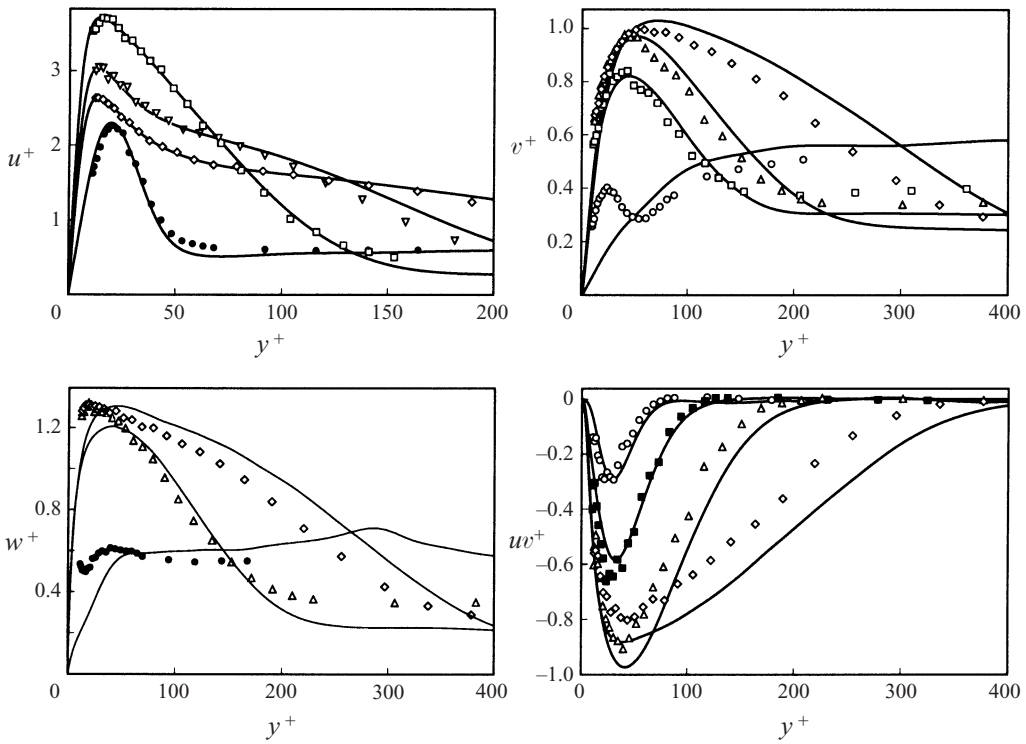

FIGURE 6. The evolution of u, v, w and $\overline{uv}$ Reynolds stress components compared to data of Roach & Brierly (1990). ○, $R_\theta = 177$; ○, $R_\theta = 225$; ■, $R_\theta = 323$; □, $R_\theta = 385$; △, $R_\theta = 539$; ◇, $R_\theta = 897$.

respects, but the slopes $\mathrm{d}C_f/\mathrm{d}x$ in the transition region are quite similar. The Rai & Moin (1993) DNS showed a rather longer transition length and a more shallow slope than experiment. That was probably due to inadequate streamwise resolution.

Mean velocity profiles at various locations in the transitional zone are compared to experimental data in figure 5. The evolution from a Blasius profile to a turbulent

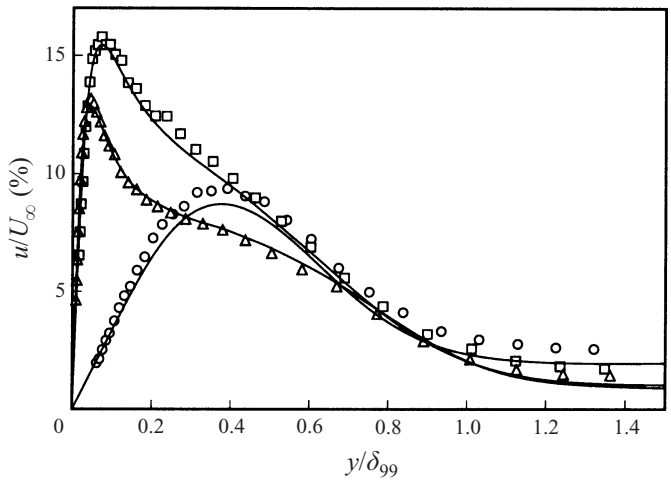

FIGURE 7. Streamwise velocity profiles, presented in the form u' versus y/δ. ○, $R_\theta = 177$; □, $R_\theta = 456$; △, $R_\theta = 711$.

profile, with a nascent logarithmic region, is portrayed by both sets of data. Other measurement stations are available for the experiments and complete fields are available for the simulations. The agreement at other locations was similar to those included in figure 5.

Figure 6 shows the development of the Reynolds stress components through transition. The streamwise intensity profiles agree quite well with experimental data. v' and w' show a discrepancy with the laboratory data at the lowest R_θ for $y_+ < 50$. The experimental data at $R_\theta = 225$ for the wall normal component, v', show a curious peak at $y_+ \approx 25$. No evidence of such behaviour is seen in the computation. Aside from this, the general evolution of the Reynolds stress tensor is the same in the DNS and experiment.

These plots in + units give a false impression that the near-wall peak in u' remains at a fixed location through transition. In fact the profile at $R_\theta = 177$ peaks near the middle of the boundary layer, while the others peak near the wall. Figure 7 distinguishes this behaviour. Here the profiles are plotted in outer-region scaling, u' versus y/δ (throughout this paper, δ is the 99% boundary layer thickness). The profiles at $R_\theta = 456$ and 711 have the aspect of turbulent flow. The profile at $R_\theta = 177$ has the shape of so-called 'Klebanoff modes' (Kendall 1991). As was discussed in the introduction, these are not modes at all, but simply terminology to categorize certain experimental data (Leib *et al.* 1999). Upstream of $R_\theta \approx 400$, when the u' profiles are plotted in the form u'/u'_{max} versus y/δ they collapse inside the boundary layer to the same Klebanoff mode form that is seen at $R_\theta = 177$ in figure 7 (Jacobs 1999). Profiles of u'/u'_{max} peak at $y/\delta \approx 0.4$ and have the same shape as $y\partial_y U$ (Goldstein & Wundrow 1998). These profiles are a Reynolds-averaged signature of the streaks discussed in § 3.2. There it is observed that the lateral streak spacing also is consistent with measurements of Klebanoff modes. Whether Klebanoff modes are a precursor to transition has been a matter of speculation. It seems clear from the results presented in the next section that they have at most a tangential relation to bypass transition. Individual, instantaneous jets in the perturbation velocity field are more likely to be the receptivity path coupling small-scale free-stream turbulence to the boundary layer. That coupling occurs very intermittently; it cannot be attributed to the ensemble-averaged notion of Klebanoff mode profiles.

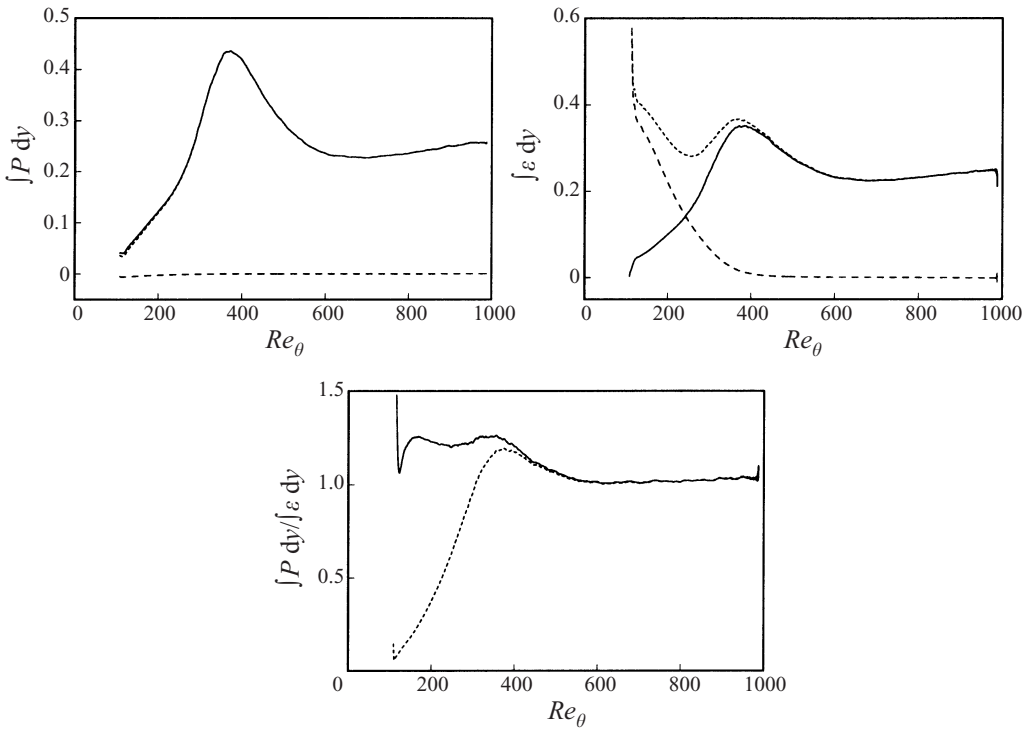

FIGURE 8. Integrated production, dissipation and their ratio. Integration over: ——, boundary layer; - - -, free stream; ····, entire domain.

As the boundary layer begins to transition, the rate of turbulent energy production rises. One way to represent this is by integrating production across the boundary layer. Integrated production is plotted in figure 8. The rate of energy dissipation also rises through transition, as shown in the figure. The integrated dissipation must be divided into a contribution from the boundary layer and a contribution from the free stream. The latter increases with the vertical domain size. The ratio of integrated production to integrated dissipation within the boundary layer falls through the transition region, as seen in figure 8. A hallmark of transition is the creation of small-scale dissipative eddies, which is why $\int P\,\mathrm{d}y/\int \varepsilon\,\mathrm{d}y$ falls. After transition this ratio is nearly unity.

3.2. *Instantaneous fields*

A curious phenomenon occurs in the laminar boundary layer upstream of the onset of transition: long streaks of u-component velocity perturbations are observed. These are seen in plan view in figure 9(a). The dark zones are regions where $u' < 0$; these intense 'negative jets' are compensated by broader regions of $u' > 0$. Figure 9 shows a segment of the computational domain within the transition region. It spans $R_\theta = 300$ to 687; the entire domain is $R_\theta = 106$ to 1000. The streaks persist into the intermittent region, where laminar and turbulent zones are juxtaposed. They continue to be seen all the way through the transition region, only terminating where the boundary layer becomes turbulent across the full span, at the right-hand side of the figure.

A patch of irregular motion is observed to develop towards the left-hand side of the upper figure, in the midst of the streaks. The time scale, T, used to label figure 9 is the interval required for the turbulent spot to travel from the location of minimum

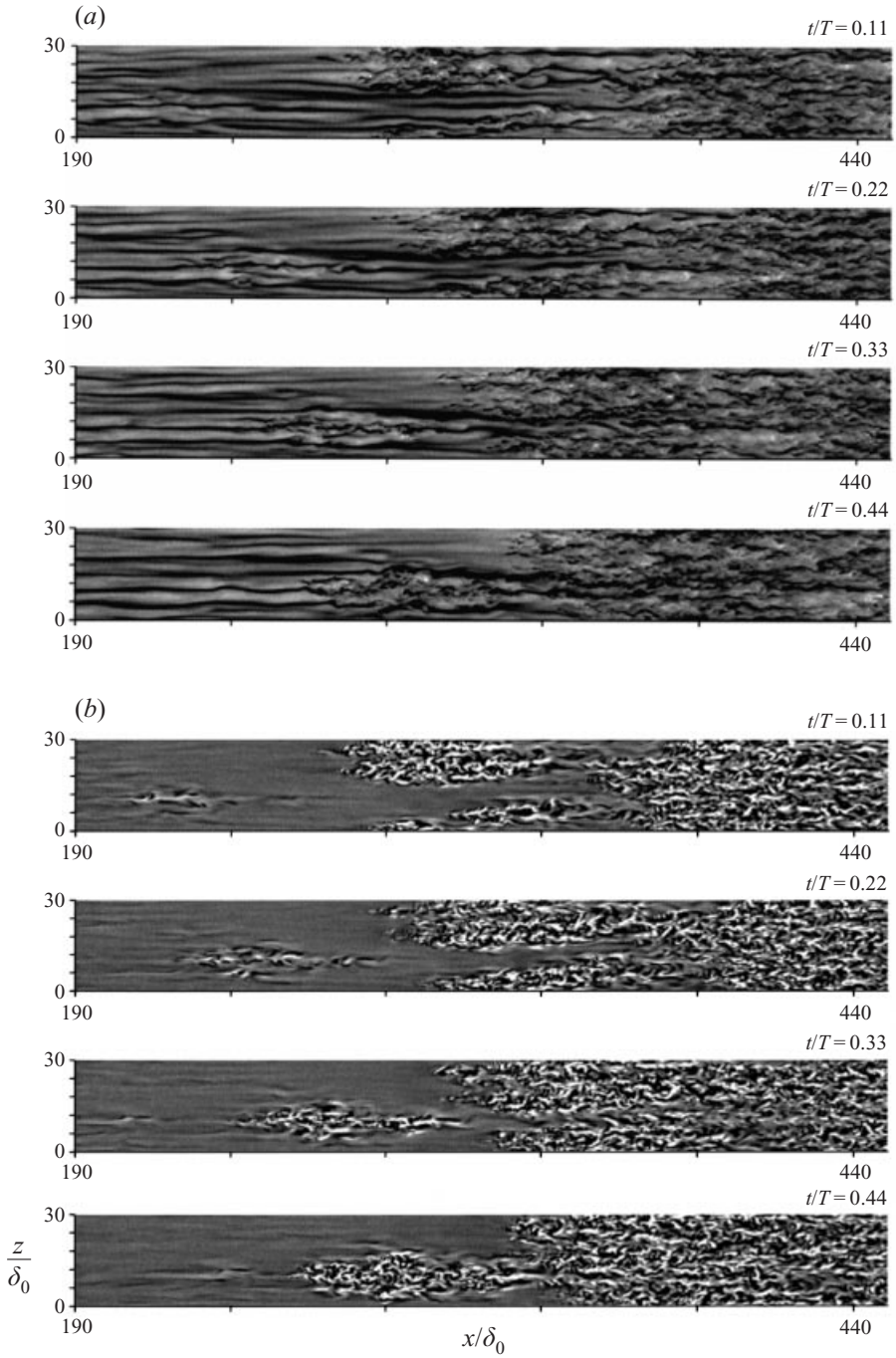

FIGURE 9. (*a*) *u*-component and (*b*) *v*-component in the (x, z)-plane. Streaks, spots and transition in a boundary layer beneath free-stream turbulence as evidenced in contours of fluctuating u and v components of velocity. Inlet $R_\theta = 300$, $y/\delta = 0.4$; exit $R_\theta = 687$, $y/\delta = 0.16$.

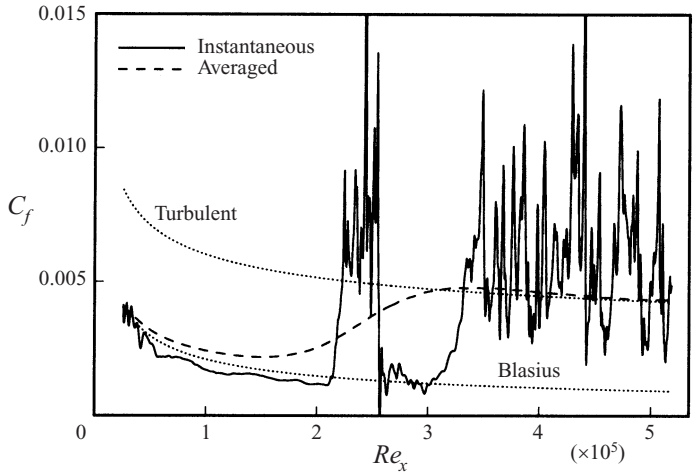

FIGURE 10. Plots of mean and instantaneous C_f versus Re_x, showing the elevated level of c_f' inside a spot.

skin friction to the location of maximum skin friction. This can be thought of as a spot lifetime; the particular sequence shown was selected to illustrate the life of a turbulent spot.

Consistent with rapid distortion theory, streaks are seen primarily in the u' component; the v' component highlights the spots. The contours of v', shown in figure 9(b), give a clearer impression of the localized nature of turbulent spots. These patches of irregular motion do not arise from a sinuous instability of a pattern of streaks; rather they appear spontaneously in a compact area. They expand rapidly in the cross-stream and streamwise direction. The front of the irregular patch propagates more rapidly than the rear, and soon overtakes the downstream fully turbulent boundary layer. The ragged edge of the turbulent zone, that can be seen in figure 9(b), is maintained by spots overtaking the main turbulent region. Without this sustenance, the turbulent zone would convect out of the computational domain, leaving a laminar, perturbed boundary layer. In time-lapse visualizations, the upstream edge of the turbulent region is seen to move slowly downstream, then to jump back as it is caught by a spot.

The spot planforms, especially that at $t/T = 0.33$, bear similarity to those obtained by Bowles & Smith (1995) through application of stationary phase to a packet of waves on a vorticity discontinuity. The lateral edges of the spot form as caustics. Toward the rear of the spot the predicted angle of the caustics is 19°, which is larger than observed. The simplifications and approximations in the analysis could well account for descrepancies. This type of analysis for top-down spots seems quite apt.

The localized nature of spots can be seen even more clearly in a plot of instantaneous skin friction versus Re_x through the middle of the spot (figure 10). The flow is laminar on either side of the instantaneously elevated pulse at $Re_x \sim 2.2 \times 10^5$. The ambient boundary layer seems to be quite stable upstream of $Re_x \sim 3 \times 10^5$. Behind the spot (i.e. upstream) the instantaneous C_f falls below the laminar level. This is probably due to the spot lying in a streak with $u' < 0$, rather than an effect of the spot *per se*.

An ensemble-averaged skin friction curve is included in figure 10. It shows that the smooth increase of C_f through the region $1.5 \times 10^5 < Re_x < 3 \times 10^5$ is a consequence of averaging a highly intermittent signal.

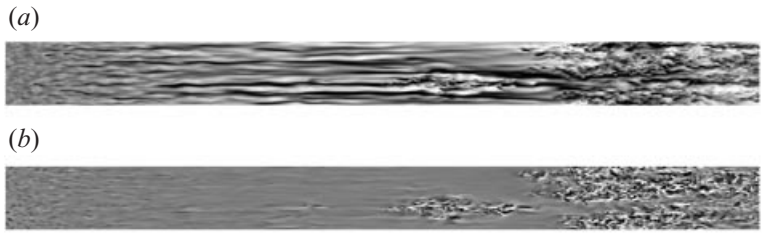

FIGURE 11. A longer section of the domain: $R_\theta = 136$ to $R_\theta = 687$. (*a*) u contours, (*b*) v contours.

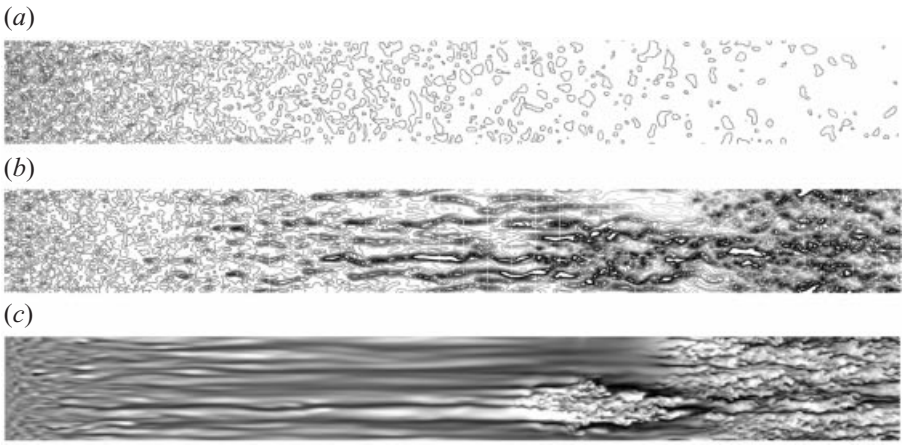

FIGURE 12. Horizontal sections through the free stream and the boundary layer. The sections are: (*a*) in the free-stream, (*b*) at $y \sim \delta$ and (*c*) at $y \sim \frac{1}{3}\delta$ where δ is the 99% thickness at $R_\theta = 250$.

Figure 11 portrays a longer portion of the flow domain than figure 9, extending from the laminar region near the inlet into the turbulent boundary layer. Relatively small-scale fluctuations are seen near the inlet. They probably have two sources. The oblique modes imposed at the inlet have an effective Reynolds number $Re\cos\gamma$. Modes with large k_z correspond to $\gamma \approx 90°$. Low-Reynolds-number Orr–Sommerfeld, continuous modes penetrate deep into the boundary layer (figure 2). Hence, highly oblique modes are seen near the inlet, but they decay rapidly. The other source of small-scale inlet boundary layer perturbations is that the form of oblique Orr–Sommerfeld modes, $e^{i\alpha(x\cos\gamma+z\sin\gamma)}$ with α complex, is not periodic in z. This is inconsistent with the specified spanwise periodic fluctuation at $x = 0$. A rapid adjustment takes place and this causes small-scale motions, that decay very quickly.

The downstream flow clearly is responding to the low-frequency components of the overlying free-stream turbulence, without contamination by inlet effects. It will be shown subsequently (figure 16) that streaks are part of this response to large-scale external eddies. The dominant streak spacing is seen to originate where these eddies penetrate the upper half of the boundary layer.

Figure 12 consists of u-velocity fluctuation contours in planes parallel to the wall: (*a*) is in the free stream, (*b*) is at the upper edge of the boundary layer, and (*c*) is near the surface. A striking qualitative change from nearly isotropic turbulence in the free stream to highly elongated streaks near the wall is observed as the plane moves down through the boundary layer. This is an illustration of shear sheltering. The rationale presented in Jacobs & Durbin (1998) for this phenomenon is that

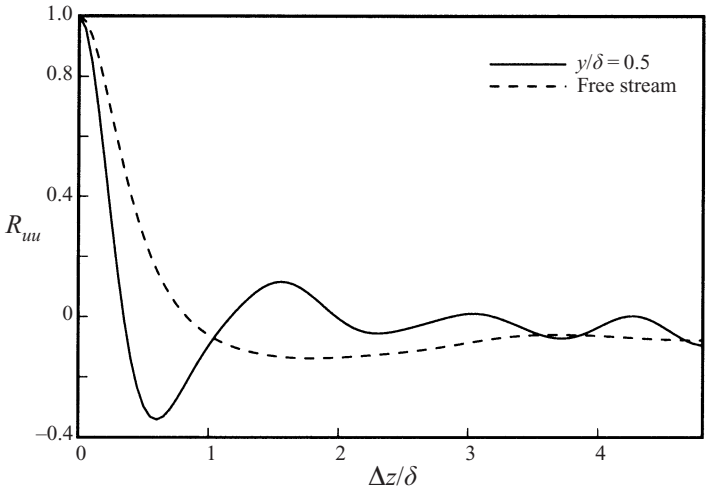

FIGURE 13. Spanwise correlation function, $R_{uu}(\Delta z)$.

modes of the continuous spectrum of the Orr–Sommerfeld equation are practically zero inside the boundary layer, unless the frequency is low. The small scales in the free stream are prevented by the mean shear from perturbing the boundary layer. The sheltering phenomenon is also known in receptivity theory (Kerschen 1991): qualitatively, disturbances convected with the free-stream velocity do not couple to the slower fluid within the boundary layer.

In the buffeted boundary layer, viscous stresses are able to withstand the free-stream perturbations and the boundary layer remains laminar. The elongated streaks originate through an elaboration of shear sheltering. The shear might better be thought of as filtering free-stream disturbances, letting low-frequency components of the external turbulence penetrate the boundary layer, while expelling higher frequencies (Jacobs & Durbin 1998; Hunt & Durbin 1999); Alfredsson & Matsubara (1996) contains experimental time traces that also are consistent with shear filtering. Upon entering the boundary layer, low-frequency disturbances are amplified by the mean shear (Andersson *et al.* 1999). The energy spectrum shifts toward even lower frequencies as nonlinearity produces difference frequencies.

Streamwise elongated streaks emerge quite generally as a feature of zero-pressure-gradient laminar boundary layers buffeted by free-stream eddies. As mentioned in connection with figure 7, streaks appear to be identical to what have been called Klebanoff modes (Kendall 1991). There we commented that the u' versus y/δ profiles have the same form as seen in experiments. Figure 13 shows the spanwise correlation $\overline{u(z+\Delta z)u(z)}/\overline{u^2}$ at $y/\delta = 0.5$. If the averaged streak spacing is defined as twice the distance to the first minimum of the correlation function, then this spacing is $\approx 1.2\delta$. That is consistent with experimental measurements (Westin *et al.* 1994). The dashed line in figure 13 shows that the spanwise structure is absent in the free stream.

Direct simulations have made a significant impact on our understanding of the process of bypass transition by enabling the early stages, before turbulent spots appear, to be explored. By the time that spots appear, a local region has already broken down to turbulence. Prior to that stage laminar, highly sheared flow patterns appear in the form of the backward jets cited previously. Irregularities similar to Kelvin–Helmholtz instability are triggered on these shear layers and at some late stage of development they become localized turbulent patches.

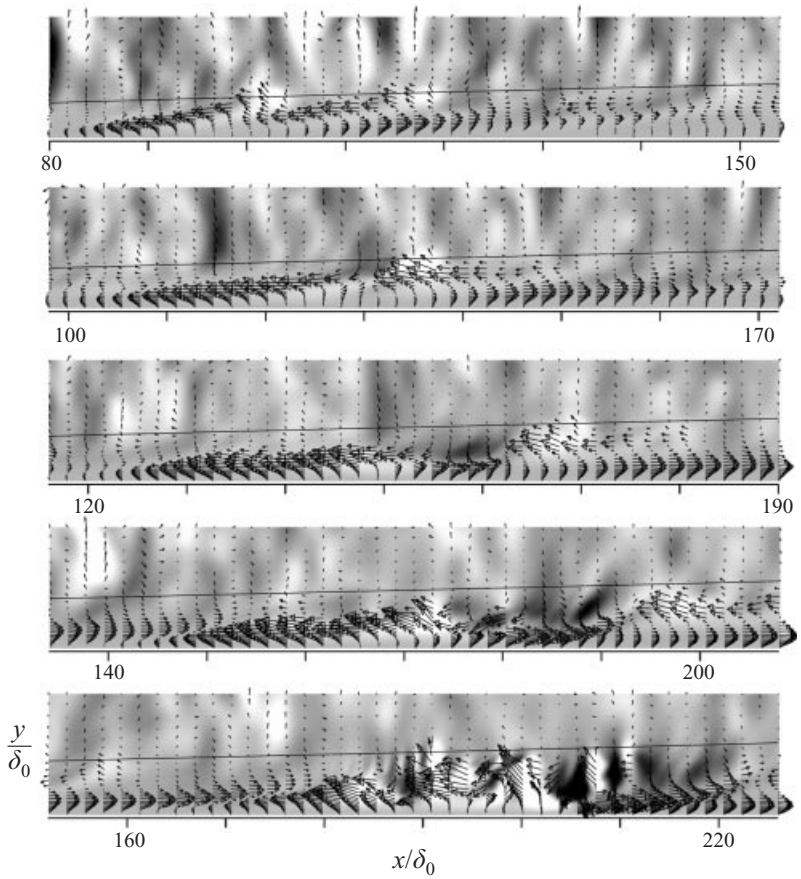

FIGURE 14. Backward jets in the (x, y)-plane. Time sequence showing the evolution of the spot precursor via vectors. The vertical scale has been expanded by a factor of 2; vector profiles are separated by 6 grid points. The viewing window moves at $0.51U_\infty$ in order to keep the perturbation in the picture. The final view is of the region $271 < R_\theta < 344$. From top to bottom, $t/T = -0.4$, -0.3, -0.2, -0.1, 0.

Figure 14 illustrates the evolution of a perturbation on a backward jet as it appears in the present simulation. The background contours show v: $v > 0$ is light, $v < 0$ is dark. The y-axis has been magnified two times for the purpose of display; the impression of anisotropy in the free stream is an artifice of this distortion. The spot that is seen in figure 11 corresponds to a time somewhat beyond those shown in figure 14: the sections of figure 14 are labelled with negative times to indicate that they show precursors to the emergence of spots in figure 9; at $t/T = 0$ a nascent spot fills the left, central region ($x/\delta_0 \approx 190$–210) of the boundary layer in the lowest panel of figure 14. After its initiation, this region of irregular motion grows rapidly and becomes visible in coarse-level contour plots.

The flow region viewed in figure 14 moves downstream at $0.51U_\infty$ in order to keep the perturbation in the picture. The final image spans the region $271 < R_\theta < 344$; the previous images cover the ranges $252 < R_\theta < 324$, $232 < R_\theta < 306$, $211 < R_\theta < 289$, and the inital image spans the region $188 < R_\theta < 271$ – essentially the right-hand edge moves in increments of $\Delta R_\theta \approx 20$.

The line across each of the plots shows where $y = \delta(x)$. A small region of flow

upward across that line is seen in the velocity vectors at $x/\delta_0 \approx 112$, $y \approx \delta$ of the top frame. This has moved to the middle of the next frame. It is the disturbance which continues to grow, filling the boundary layer with a strip of irregular velocity vectors at $t/T = 0$.

Both here and in Wu *et al.* (1999) the jets that precede turbulent spots are located in the upper part of the boundary layer. It appears that backward jets constitute low-speed fluid that was lifted from near the wall. The numerical data show a correspondence between negative jets and upward v velocity. In the initial stages, that upwelling appears to be associated with large-scale free-stream eddies. The spanwise spacing seems to be filtered from the external perturbation.

Forward jets are seen close to the wall. These can be quite intense, reaching 25% of the free-stream velocity. They are generally broader in the z-direction than the negative jets, possibly because they are produced by downward flow which is blocked by the wall. Forward jets seem never to be the seat of breakdown. This is further evidence that the jet must lift into the outer region of the boundary layer and be disturbed by small-scale free-stream turbulence in order to breakdown.

One might question whether the eruption portrayed in figure 14 arose out of the interaction of a jet with an external eddy, or whether it is a feature of an instability, that could be stimulated by any infinitesimal perturbation. The answer to this question is found from the earlier time history.

In the uppermost views of figure 14, a white patch is seen in the free stream at $x/\delta_0 \approx 112$, $y \approx \delta$, where the velocity vectors show the upward eruption across δ. By tracing that patch to earlier times, it was seen to exist and to be located in the free stream prior to the eruption. It can be surmised that the breakdown to irregular motion seen toward the bottom of this figure originated where a backward jet was highly perturbed by a free-stream eddy. The complex process by which free-stream turbulence enters the boundary layer is twofold: firstly, low-frequency eddies produce a lifted, backward jet; secondly, smaller scales disrupt that jet. Smaller scale motions then develop within the jet shear layer. This and similar visualizations are evidence that the breakdown occurs only near the top of the boundary layer. External disturbances do not penetrate the boundary layer; rather, the backflow jet rises to the boundary layer edge, then it bursts. The nonlinear theory of Li *et al.* (1998) envisions a breakdown of this form.

Of the jets observed, most do not spawn spots. We have not discovered a definite qualitative signature of those jets that become spot precursors. They must be of sufficient amplitude and they must be located in the outer portion of the boundary layer. Perhaps a threshold level of shear is required; perhaps a threshold level of perturbation is needed. Clearly it is not simply a matter of the jet profile implying instability; there is also a requirement of coupling to free-stream eddies. The backward jet provides a local receptivity path; it also provides an inviscidly unstable, inflectional profile. When the jets lift into the upper half of the boundary layer, they are no longer sheltered by the shear from small-scale free-stream turbulence. This seems to be an element of their responsiveness. However, the higher disturbance simulations in § 4 suggest that a threshold level of perturbation still is needed to stimulate rapid breakdown into a patch of turbulence.

A plan view of a portion of the computational domain contains backward jets dispersed throughout the buffeted laminar boundary layer (figure 15). Views at later times reveal that most of them do not develop turbulent spots. The location of the jet in figure 14 that does produce a spot is indicated by an arrow at the left of figure 15. Figure 15 provides data on the three flow components in the plane visualized. The

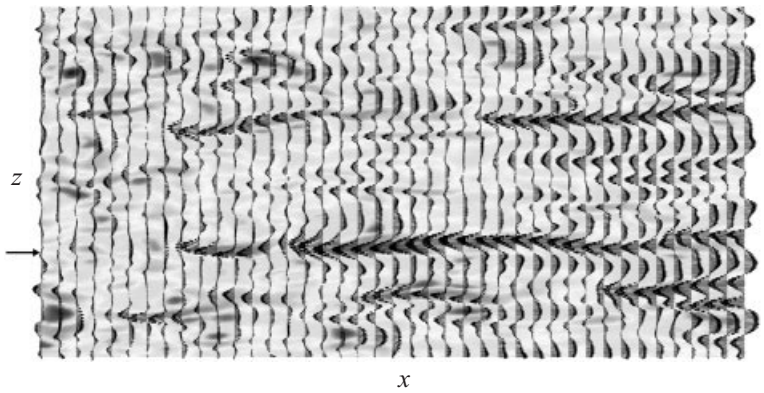

FIGURE 15. Velocity vectors in the (x,z)-plane. The constant y-plane corresponds to $y/\delta = 0.6$ at the left-hand edge and $y/\delta = 0.53$ at the right. The region shown is from $R_\theta = 163$ to $R_\theta = 239$. The v component is contoured in the background.

dark background shows where v' is negative; the light background is where it is positive. Negative jets are usually in a region of $v > 0$. A flow divergence in the plane seems to be associated with the localized breakdown.

Distinct asymmetry is exhibited between narrow, intense jets of negative u' and broad, weak regions of positive u'. It seems to be critical to the overall process of transition. Asymmetry can be rationalized by arguing that upward convection of low-momentum fluid causes the negative jet. As this fluid lifts up it has an increasingly intense negative velocity relative to the ambient mean velocity. Jets in the outer portion of the boundary layer are predominantly negative because upward motion produces them and moves them there. Positive jets form in downward motion, and are seen near the wall in figure 14.

The side and top views presented so far provide compelling evidence of that transition originates in the upper boundary layer. The final perspective is the end view. End views looking downstream are contained in figure 16. The horizontal axis is labelled in units of the inlet boundary layer thickness (δ_0); a useful conversion factor is the corresponding inlet Reynolds number, $R_{\delta_0} = 798$ or $R_x = 2.55 \times 10^4$. These panels show how negative jets originate near the wall where large-scale free-stream eddies penetrate the boundary layer. The shading contours the u-component of velocity. Positive jets (white patches) stay near the surface. Negative jets (dark) lift up, sometimes moving over top of a positive jet. Negative jets overlying positive jets seem to be the most unstable. The large black regions, seen to be rising over the white ellipse near $z/\delta_0 = 10$, toward the left of figure 16, subsequently explode into a patch of turbulence.

The arrow on the left of figure 16 indicates $y = \delta$. Large free-stream eddies are seen to cross this level in the $R_\theta = 222$ view. They clearly are the origin of the regions of positive and negative u near the wall; they initiate the streaks. The spacing between light and dark patches increases downstream, providing evidence that the streak spacing is selected within the boundary layer. The final data, at $R_\theta = 403$, show how the disruption penetrates to the wall as the disturbance moves downstream.

3.3. *Spectra*

Frequency spectra are not usually computed from DNS because they require a long integration time. The low frequencies, especially, are subject to inaccuracies of short

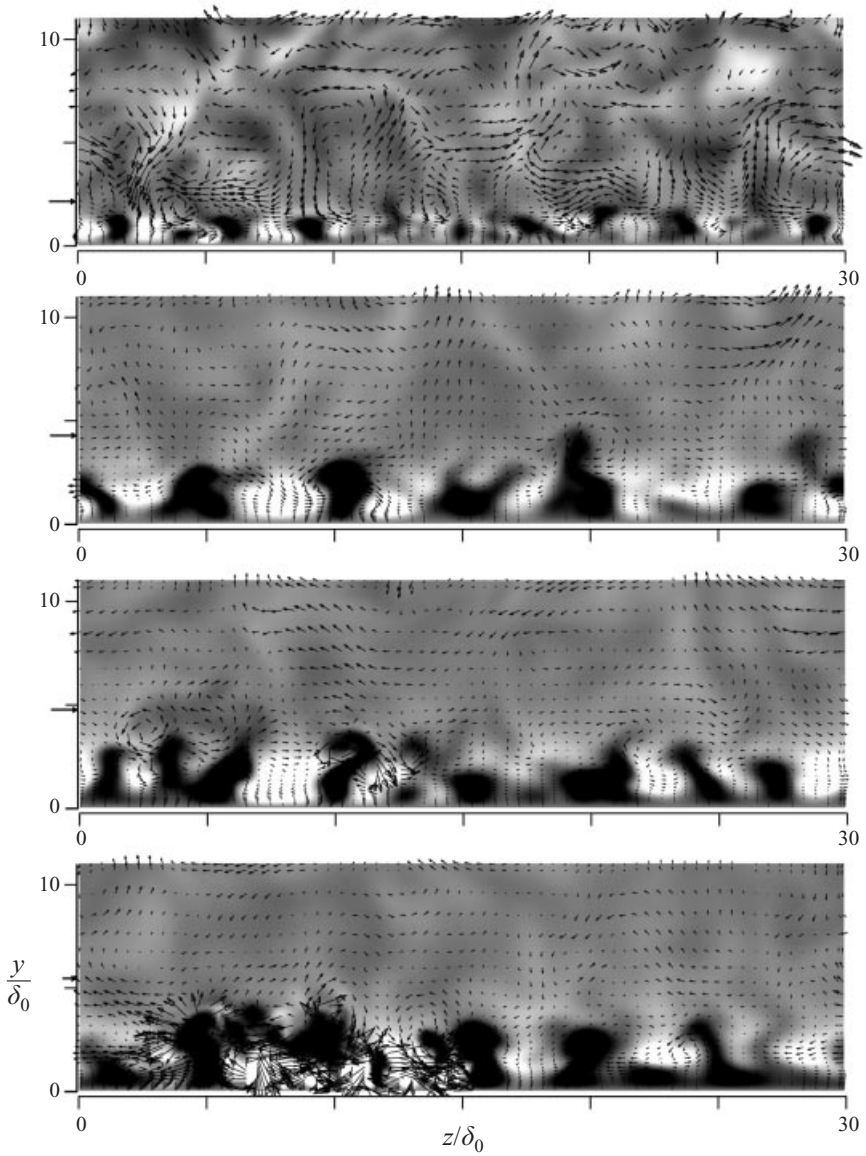

FIGURE 16. End view of the (y, z)-plane. The u component is contoured. Light regions are positive, dark are negative. The arrow marks the local 99% thickness. Sequence of sections at $R_\theta = 222, 331, 364$ and 403.

sampling time. The present spectra serve to illuminate characteristics of the laminar boundary layer response to free-stream turbulence. To that end, they are deemed sufficiently accurate.

Energy frequency spectra,

$$\int_{-\infty}^{\infty} \overline{u(t)u(t+\tau)}\, \mathrm{e}^{\mathrm{i}\omega\tau}\, \mathrm{d}\tau,$$

at three downstream locations are shown in figure 17. The synthetic inlet spectrum is that at $R_\theta = 106$. It looks jagged because the number of frequencies included

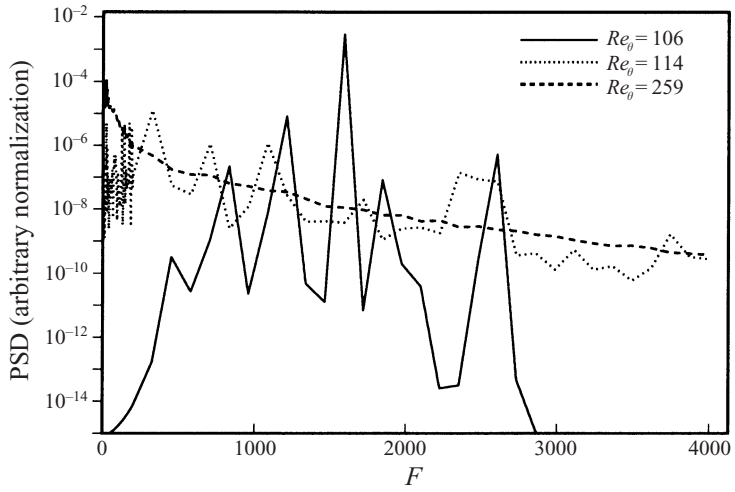

FIGURE 17. Energy spectra, $E(\omega)$ at $R_\theta = 106$ (——), 114 (····) and 259 (- - -). $y/\delta \sim 0.25$, showing development of very low frequencies. $F = 10^6\omega\nu/U_\infty^2$.

at the inlet is small. The lowest frequency in the synthesized inlet spectrum is far higher than the dominant frequencies in the region of laminar streaks, represented by the spectrum at $R_\theta = 259$. Frequencies below those introduced at the inlet are generated by nonlinear interactions. The dominant frequencies at $R_\theta = 259$ are below $F \equiv 10^6\omega\nu/U_\infty^2 = 40$. These frequencies were not present at the inlet. The fact that they rapidly become dominant shows the laminar boundary layer to be highly responsive at these frequencies. This answers a question that has been debated in connection with laminar region streaks: are they caused by the externally imposed disturbance, or are they an implicit property of the boundary layer? The answer seems clear: while broad-band, free-stream turbulence of sufficient amplitude is a critical input, frequency selection occurs within the boundary layer; streaks are an implicit property of the boundary layer.

The spanwise spatial spectrum,

$$\int_{-\infty}^{\infty} \overline{u(z)u(z+\zeta)}\, \mathrm{e}^{\mathrm{i}\beta\zeta}\, \mathrm{d}\zeta,$$

shows a similar shift toward low wavenumbers downstream of the inlet. The inlet spectrum is broad. Energy rapidly focuses into low-wavenumber modes with downstream distance. The contours in figure 18 are restricted to the low-wavenumber region. At the inlet there is almost no energy in this range. For purposes of display the very low-energy region at the inlet ($R_\theta \approx 100$) is shown in grey; it is not consistent with the contouring in the rest of the figure (it is actually coloured yellow). The zone of maximum E has been highlighted as an encircled patch of white in the lower, central part of the figure. The contours show that a selection process causes the spectrum to peak near $\beta\delta \sim 1.4$ and $R_\theta \sim 360$. The y variation plotted in Jacobs (1999) shows that the long-wavelength energy is highest in the lower half of the boundary layer, with its maximum at about $y/\delta \sim 0.3$.

The dominant wavelength $\beta\delta \sim 1.4$ is roughly consistent with the optimal growth hypothesis of Butler & Farrell (1992), Andersson *et al.* (1999) and others. Shear amplification causes non-modal growth of streamwise elongated disturbances, but does not select a spanwise wavelength. When viscous dissipation is added, short

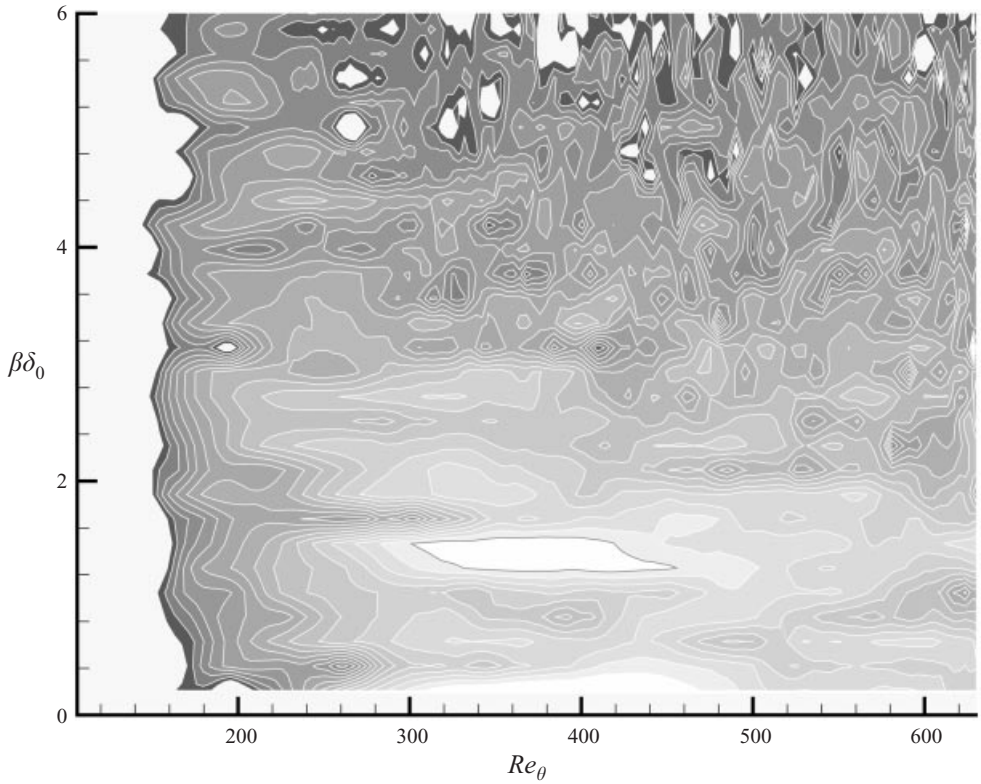

FIGURE 18. Contours of $E(\beta; x)$ in the streak region, showing selection of spanwise wavelength. $y/\delta_0 = 0.8$; $F = 11$. The grey shading to the left is a region of very low E.

spanwise wavelengths decay. The hypothesis of Butler & Farrell (1992) and Andersson *et al.* (1999) is that at any downstream position the observed disturbance will be that which experiences maximum growth from the inlet to the observation point, under the combined action of shear amplification and viscous decay. A band of dominant wavelengths is selected by this mechanism. The band of wavelengths permits the streak field to be chaotic with the impression of a spanwise period, as in illustrations presented in § 3.2. Our data and these theories support a conclusion that the dominant wavelength is selected by the boundary layer and is not sensitive to the details of the inlet disturbance, provided that it is broad band. Given a broad-band inlet, difference wavenumbers created by nonlinearity fill in the long-wavelength spectrum.

It should be emphasized, however, that the dominant β, or the averaged streak spacing, plays little role in bypass transition. The instantaneous field of backward jets is highly irregular (figure 15) and spot inception occurs locally on isolated jets.

4. Higher inlet turbulence

Auxilliary simulations were performed with an inlet turbulence intensity of 7%. The inlet boundary layer thickness was $R_\theta = 51$, and the grid dimensions were $1024 \times 240 \times 128$. The decay exponent of the free-stream intensity was $n = 0.79$, a bit higher than $n = 0.71$ for the $Tu = 3.5\%$ case. Further details are contained in Jacobs (1999).

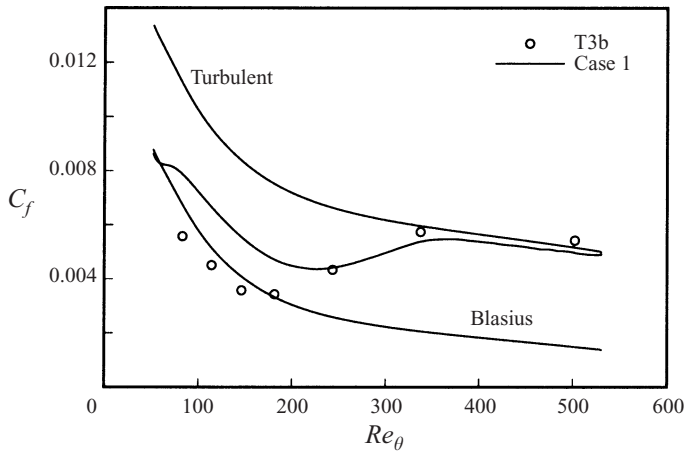

FIGURE 19. Momentum thickness and skin friction with 7% FST.

Only limited results will be presented for this case. Transition took place fairly close to the inflow boundary. However, the flow development did not show contamination by spurious coupling between free-stream turbulence and boundary layer fluctuations at the inlet. Figure 19 shows skin friction versus R_θ for the 7% case. Although a high level of C_f exists in the buffeted boundary layer, a clear transition takes place farther downstream near $R_\theta = 200$. The experimental data are from case T3b of Roach & Brierly (1990). The laboratory data follow the laminar line quite closely in the upstream, buffeted region, unlike the DNS.

Distinct spots are difficult to discern under the elevated free-stream turbulence (figure 20). Nevertheless, transition in the higher intensity case follows a course similar to that described previously, although in a higher level of ambient disturbance. The streaks and backward jets remain and the jets still provide the critical path for small-scale disturbances to enter the boundary layer and provoke transition. However, now these mechanisms take place in a high level of ambient disturbance.

Figure 20 is a slice through the flow near to the wall. Part (*a*) shows that long streaks of positive and negative u are present; positive jets are the more intense because this plane is near the surface. Regions of irregular motion can be seen in the vector plot: these occur at the lower left, central and upper right and in the middle of the figure. So there are at least four turbulent spots between $R_\theta = 125$ and $R_\theta = 265$. At the lower intensity we have never seen more than one spot in a region this small.

Spots appear to form, but there are more of them per unit area and they merge with each other at an early stage. Figure 20(*b*) is a magnified view of the spot at right centre of the upper plot. It suggests a similar type of disruption to that seen at lower intensity.

The increased area density of spots with increased turbulence intensity suggests that there is a threshold amplitude for spots to form. This is a telling observation: it implies that the breakdown involves a nonlinear instability process. The higher level of free-stream disturbance overcomes the instability threshold more frequently than in the lower intensity case.

5. Conclusion

These direct simulations are essentially experiments, albeit performed on a computer. Extensive grid refinement studies give confidence that the results are not

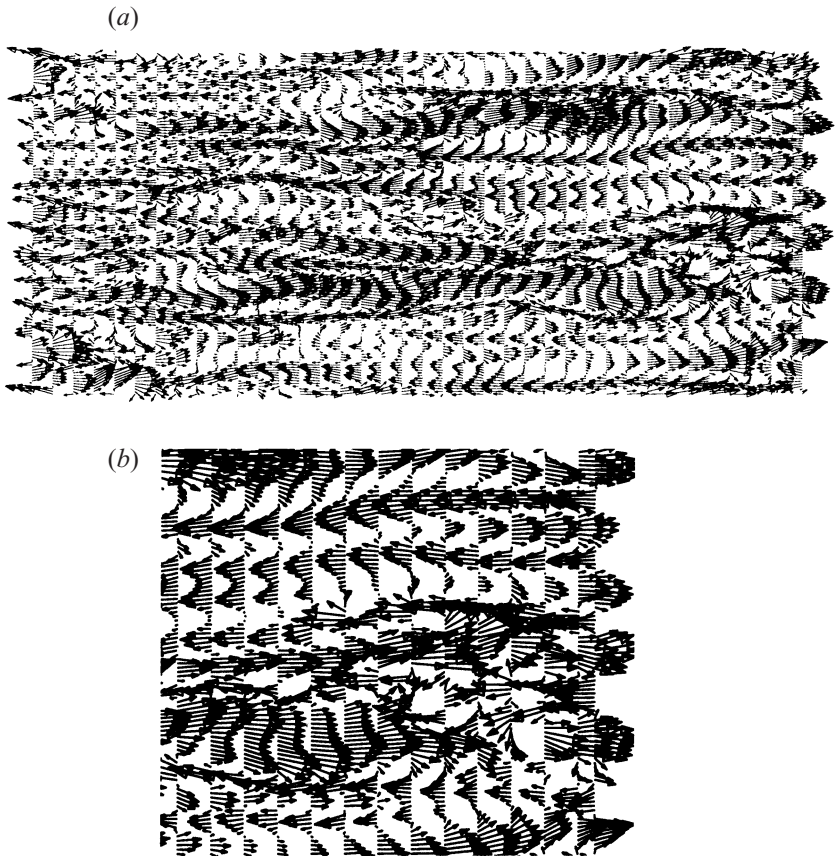

FIGURE 20. Streaks and spots with 7% FST. Inlet $R_\theta = 125$, $y/\delta = 0.24$ ($y_+ = 14.3$); exit $R_\theta = 265$, $y/\delta = 0.11$ ($y_+ = 12.7$). (*a*) Velocity vectors in the (x, z)-plane. (*b*) A zoom of the spot at right centre.

contaminant by finite domain width or by inadequate grid resolution. In addition to the refinement studies presented here, Jacobs (1999) reports full domain simulations on coarser meshes. The most sensitive quantity is skin friction: a simulation with 1536 points in the streamwise direction slightly overpredicted C_f in the turbulent region; figure 4 shows that with 2048 points it has become quite accurate. Within the bounds implied by these checks, our results can be considered experimentally accurate.

Laboratory experiments have not completly elucidated the mysterious bypass mechanisms. The present data provide a more comprehensive picture. The process has several subtleties. Long streaks of streamwise velocity perturbation are initiated by penetration of low-frequency modes from the free-stream. Their spectrum evolves and a new spectrum with energy dominated by quite low frequencies is established through nonlinearity. This seems to be a selection process that occurs in the shear layer, and that removes sensitivity to details of the inlet spectrum.

The near-wall streaks do not undergo instability; indeed they seem to be remarkably stable as long as they remain in the lower part of the boundary layer. However, when upwelling lifts them from the surface they become a receptivity site for smaller scale free-stream turbulence which initiates an instability near the top of the boundary layer. This disturbance grows rapidly, filling the boundary layer with a patch of irregular

motion. Subsequently this local breakdown becomes recognized as a turbulent spot. The spots continue to grow until they merge with the downstream, fully turbulent region. Merging maintains the upstream edge of the turbulent region.

One might wonder whether there is any connection between the laminar and turbulent region streamwise velocity streaks. It might not be clear from the data presented herein, but the streaks are disrupted at transition and those which appear in the fully turbulent zone are not a continuation from upstream.

This work was supported by the Office of Naval Research, grant #N00014-99-1-0300.

REFERENCES

Akselvoll, K. & Moin, P. 1996 Large eddy simulation of turbulent confined coannular jets. *J. Fluid Mech.* **315**, 387–411.

Alfredsson, P. H. & Matsubara, M. 1996 Streaky structures in transition. In *Transitional Boundary Layers in Aeronautics* (ed. Henkes & van Ingen), pp. 374–386. Elsevier.

Andersson, P., Berggren, M. & Henningson, D. S. 1999 Optimal disturbances and bypass transition in boundary layers. *Phys. Fluids* **11**, 134–150.

Bowles, R. G. A. & Smith, F. T. 1995 Short-scale effects on model boundary-layer spots. *J. Fluid Mech.* **295**, 395–407.

Butler, K. M. & Farrell, B. F. 1992 Three-dimensional optimal disturbances in viscous shear flow. *Phys. Fluids* A **4**, 1637–1650.

Drazin, P. & Reid, W. H. 1995 *Hydrodynamic Stability*. Cambridge University Press.

Elofsson, P. A., Kawakami, M. & Alfredsson, P. H. 1999 Experiments on the stability of streamwise steaks in plane Poiseuille flow. *Phys. Fluids* **11**, 134–150.

Goldstein, M. E. & Wundrow, D. W. 1998 On the environmental realizability of algebraically growing disturbances and their relation to Klebanoff modes. *Theoret. Comput. Fluid Dyn.* **10**, 171–186.

Grosch, C. E. & Salwen, H. 1978 The continuous spectrum of the Orr–Sommerfeld equation. Part 1. The spectrum and the eigenfunctions. *J. Fluid Mech.* **87**, 33–54.

Hunt, J. C. R. & Carruthers, D. J. 1990 Rapid distortion theory and the 'problems' of turbulence. *J. Fluid Mech.* **84**, 209–235.

Hunt, J. C. R. & Durbin, P. A. 1999 Perturbed shear layers. *Fluid Dyn. Res.* **24**, 375–404.

Jacobs, R. G. 1999 Bypass transition phenomena studied by numerical simulation. PhD thesis (report TF-77), Stanford University.

Jacobs, R. G. & Durbin, P. A. 1998 Shear sheltering and the continuous spectrum of the Orr–Sommerfeld equation. *Phys. Fluids* **10**, 2006–2011.

Kendall, J. M. 1991 Studies on laminar boundary layer receptivity to free stream turbulence near a leading edge. In *Boundary Layer Stability and Transition to Turbulence* (ed. Reda *et al.*). ASME-FED Vol. 114, pp. 23–30.

Kerschen, E. J. 1991 Linear and nonlinear receptivity to vortical free-stream disturbances. In *Boundary Layer Stability and Transition to Turbulence* (ed. Reda *et al.*). ASME-FED Vol. 114, p. 43.

Kleiser, L. & Zang, T. A. 1991 Numerical simulation of transition in wall-bounded shear flows. *Ann. Rev. Fluid Mech.* **23**, 495–537.

Lee, M. J., Kim, J. & Moin, P. 1990 Structure of turbulence at high shear rate. *J. Fluid Mech.* **216**, 561–583.

Leib, S. J., Wundrow, D. & Goldstein, M. E. 1999 Effect of free-stream turbulence and other vortical disturbances on a laminar boundary layer. *J. Fluid Mech.* **380**, 169–203.

Li, L., Walker, J. D. A., Bowles, R. I. & Smith, F. T. 1998 Short-scale break-up in unsteady interactive layers: local development of normal pressure gradients and vortex wind-up. *J. Fluid Mech.* **374**, 335–378.

Luchini, P. 2000 Reynolds number independent instability of the boundary layer over a flat surface: optimal perturbations. *J. Fluid Mech.* **404**, 289–309.

Phillips, O. M. 1969 Shear-flow turbulence. *Ann. Rev. Fluid Mech.* **1**, 245–264.

Pierce, C. D. & Moin, P. 1998 Large eddy simulation of a confined coaxial jet with swirl and heat release. *AIAA Paper* 98-2892.

Rai, M. M. & Moin, P. 1993 Direct numerical simulation of transition and turbulence in a spatially evolving boundary layer. *J. Comput. Phys.* **109**, 169–192.

Reddy, S. C., Schmid, P. J., Baggett, J. S. & Henningson, D. S. 1998 On stability of streamwise streak and transition thresholds in plane channel flows. *J. Fluid Mech.* **365**, 269–303.

Reshotko, E. A. 1976 Boundary layer stability and transition. *Ann. Rev. Fluid Mech.* **8**, 311–349.

Roach, P. E. & Brierly, D. H. 1990 The influence of a turbulent freestream on zero pressure gradient transitional boundary layer development, part I: test cases T3A and T3b. *ERCOFTAC Workshop: Numerical Simulation of Unsteady Flows and Transition to Turbulence, Lausanne, Switzerland*, pp. 319–347. Cambridge University Press.

Rogallo, R. S. 1981 Numerical experiments in homogeneous turbulence. *NASA Tech. Memo.* 81315.

Savill, A. M. 1996 One point closures applied to transition. In *Turbulence and Transition* (ed. Hallbäck *et al.*), pp. 233–268. Kluwer.

Tam, C. K. W. 1978 Excitation of instability waves in a two-dimensional shear layer by sound. *J. Fluid Mech.* **81**, 357–371.

Westin, K. J. A., Boiko, A. V., Klingmann, B. G. B., Kozlov, V. V. & Alfredsson, P. H. 1994 Experiments in a boundary layer subjected to freestream turbulence. Part I: boundary layer structure and receptivity. *J. Fluid Mech.* **281**, 193–218.

Wu, X., Jacobs, R. G., Hunt, J. C. R. & Durbin, P. A. 1999 Simulation of boundary layer transition induced by periodically passing wakes. *J. Fluid Mech.* **398**, 109–153.

Van Dyke, M. 1982 *An Album of Fluid Motion.* The Parabolic Press.

Yang, Z. & Voke, P. 1995 Numerical study of bypass transition. *Phys. Fluids* **7**, 2256–2264.